Journal of Taibah University for Science

ISSN: (Print) (Online) Journal homepage: www.tandfonline.com/journals/tusc20

Sonosynthesis and artificial intelligence-enhanced characterization of PEGylated *Camellia sinensis*-encapsulated zinc oxide nanoparticles: cytotoxicity capacity against cervical cancer and fibroblast cells

Anıl Asmaz, Fulya Ustun-Alkan, Ismail Bergutay Kalaycilar, Tarik Kucukdeniz, Fatih Özbaş & Selcan Karakuş

To cite this article: Anıl Asmaz, Fulya Ustun-Alkan, Ismail Bergutay Kalaycilar, Tarik Kucukdeniz, Fatih Özbaş & Selcan Karakuş (2024) Sonosynthesis and artificial intelligence-enhanced characterization of PEGylated *Camellia sinensis*-encapsulated zinc oxide nanoparticles: cytotoxicity capacity against cervical cancer and fibroblast cells, Journal of Taibah University for Science, 18:1, 2363579, DOI: 10.1080/16583655.2024.2363579

To link to this article: https://doi.org/10.1080/16583655.2024.2363579

© 2024 The Author(s). Published by Informa UK Limited, trading as Taylor & Francis Group.

Published online: 08 Jun 2024.

Submit your article to this journal

Article views: 123

View related articles

View Crossmark data

Full Terms & Conditions of access and use can be found at
https://www.tandfonline.com/action/journalInformation?journalCode=tusc20

JOURNAL OF TAIBAH UNIVERSITY FOR SCIENCE
2024, VOL. 18, NO. 1, 2363579
https://doi.org/10.1080/16583655.2024.2363579

OPEN ACCESS Check for updates

Sonosynthesis and artificial intelligence-enhanced characterization of PEGylated *Camellia sinensis*-encapsulated zinc oxide nanoparticles: cytotoxicity capacity against cervical cancer and fibroblast cells

Anıl Asmaz[a], Fulya Ustun-Alkan[b], Ismail Bergutay Kalaycilar[c,d], Tarik Kucukdeniz[e], Fatih Özbaş[f] and Selcan Karakuş[a]

[a]Department of Chemistry, Faculty of Engineering, Istanbul University-Cerrahpaşa, Istanbul, Türkiye; [b]Department of Pharmacology and Toxicology, Faculty of Veterinary Medicine, Istanbul University-Cerrahpaşa, Istanbul, Türkiye; [c]Department of Biochemistry, Faculty of Veterinary Medicine, Istanbul University-Cerrahpaşa, Istanbul, Türkiye; [d]Institute of Nanotechnology and Biotechnology, Istanbul University-Cerrahpaşa, Istanbul, Türkiye; [e]Department of Industrial Engineering, Faculty of Engineering, Istanbul University-Cerrahpaşa, Istanbul, Türkiye; [f]Research Center for the Conservation of Cultural Property of Foundation, Fatih Sultan Mehmet Vakif University, Istanbul, Türkiye

ABSTRACT

In this study, we investigated the cytotoxicity of zincoxide nanoparticles (ZnO NPs) encapsulated in PEGylated *Camellia sinensis* extract (CL) against L929 fibroblasts and HeLa cervical cancer cells. Characterization results revealed that the CL/ZnO NPs maintained a spherical morphology with an average diameter of 40 ± 5 nm. Moreover, advanced computer vision and texture analysis have provided intricate details regarding the surfaces of CL/ZnO NPs, revealing crucial morphological features and distribution patterns that are essential for understanding their interactions with cellular structures. Statistical evaluation revealed a pronounced cytotoxic effect of CL/ZnO NPs on HeLa cells, with IC50 values of 13.708 $\mu g\ mL^{-1}$ at 48 hours, compared to $> 100\ \mu g\ mL^{-1}$ for L929 cells, indicating selective anti-cancer activity of NPs with minimal impact on fibroblast cells. These findings not only highlight CL/ZnO NPs as effective candidates for anti-cancer therapy but also highlight the synergistic power of combining biotechnology with AI-driven imaging for cancer treatments.

ARTICLE HISTORY
Received 8 March 2024
Revised 28 May 2024
Accepted 30 May 2024

KEYWORDS
ZnO nanoparticles; *Camellia sinensis*; biological assessment; artificial intelligence characterization; sustainable nano-drug carriers

1. Introduction

The use of nanoscience is rapidly expanding across a broad spectrum of scientific disciplines, encompassing biology, chemistry, physics, materials science, environmental science, and pharmaceuticals. Nanostructures exhibit diverse applications, including antibacterial, anti-cancer, and photocatalytic activities, which are enabled by their unique characteristics, shaped by their size and shape. The development and design of materials within the 1–100 nm size range are central to the burgeoning fields of nanoscience and nanotechnology [1–7]. In recent years, inorganic nano-drug carriers have gained popularity because of their potential to provide long-term green solutions to a wide range of issues [8–14]. One area of study is the fabrication of nanostructures using sustainable chemical methods involving the use of organic compounds or natural extracts from biomass [15–18]. Given that tea is one of the most widely consumed beverages worldwide, its potential health benefits have been extensively studied [19]. Tea polyphenols, known for their anti-inflammatory, antioxidant, and anti-cancer activities [20–23], can be incorporated into metal/metal oxide-based nanoparticles (NPs) to enhance their properties [24–29]. This approach enables the development of sustainable nano-drug carriers with improved medicinal properties. Consequently, the integration of sustainable chemistry with nanostructures holds promising for the development of innovative and potent treatment strategies for various diseases in nanotechnology [30–32].

Matcha powder is derived from *Camellia sinensis* and is known to contain high levels of bioactive components, including catechin, theanine, and caffeine, which have been found to exhibit antioxidant, anti-inflammatory, and anti-cancer properties. These bioactive components act as natural cytotoxic compounds that inhibit cancer cell growth, making them effective therapeutic options for cancer treatment [33–37]. Studies have shown that matcha can effectively inhibit the growth of cancer cells in various types of cancers, including prostate, breast, and lung [38,39]. *Camellia sinensis* is a member of the Theaceae family and is widely cultivated to produce tea in many regions, such as Turkey, Japan, China, Sri Lanka, and India. Natural leaves are used to produce several types of biomasses, including green, black, white, and oolong tea, which

CONTACT Selcan Karakuş selcan@iuc.edu.tr Department of Chemistry, Faculty of Engineering, Istanbul University-Cerrahpaşa, 34320 Avcilar, Türkiye

© 2024 The Author(s). Published by Informa UK Limited, trading as Taylor & Francis Group.
This is an Open Access article distributed under the terms of the Creative Commons Attribution License (http://creativecommons.org/licenses/by/4.0/), which permits unrestricted use, distribution, and reproduction in any medium, provided the original work is properly cited. The terms on which this article has been published allow the posting of the Accepted Manuscript in a repository by the author(s) or with their consent.

are also known for their biomedical effects. Studies have revealed that *Camellia sinensis* possesses antioxidant, anti-inflammatory, and anti-cancer properties, and green tea is a well-known source of health benefits [34,35].

Green nanoparticles (NPs) have garnered considerable attention in the field of pharmaceutical nanotechnology, especially due to their sustainable utilization in various biomedical applications [40–46]. ZnO is one of the most frequently studied nano-drug carriers among metal oxides and bio-matrices, owing to its remarkable chemical, physical, and biological properties. According to previous studies, oxidative stress, DNA damage, and mitochondrial malfunction are processes through which green ZnO NPs induce apoptosis and decrease cancer cell growth [47–49]. In addition, studies in animal cancer models have demonstrated the efficacy of ZnO NPs in reducing cancer growth and preventing metastasis [50–52]. Jevapatarakul et al. developed a combination of *Cratoxylum formosum* crude extract and ZnO nanosheets and investigated its impact on non-melanoma skin cancer cells [53]. Researchers have discovered that it demonstrates notable biological activity against non-melanoma skin cancer cells as it suppresses cancer cell growth and induces cell death. It is important to note that while Eswari et al. found that green-synthesized ZnO NPs using *Abutilon Indicum* and *Tectona Grandis* leaf extracts exhibited potential for their potential anti-diabetic, anti-inflammatory, and cytotoxic activities, further research is needed to validate the safety and efficacy of these ZnO NPs in animal and human studies [54]. In 2017, Nava et al. utilized a hydrothermal method at high temperature (400°C, 2 h) to synthesize ZnO NPs encapsulated in *Camellia sinensis* extract (CL). However, their focus was primarily on the synthesis and characterization processes [55]. Conversely, Çolak employed a solvent method to fabricate ZnO NPs at a high temperature (100°C and $Zn(Ac)_2{\cdot}2H_2O$) with a similar emphasis on characterization [56]. In contrast to previous literature, our study aimed to achieve a practical and cost-effective solution for synthesizing ZnO NPs in green extract using a sonochemical method at room temperature (30 min), bypassing the need for high temperatures. While previous research has concentrated on synthesis and characterization, our study delved into a detailed examination of the cytotoxic effects of CL/ZnO NPs on L929 fibroblasts and HeLa cervical cancer cells. The objective of our study was to adopt an energy-saving approach compared to traditional synthesis methods and utilize artificial intelligence (AI)-supported methods to assess the potential of CL/ZnO NPs for cancer treatment. These results suggest that CL/ZnO NPs show potential as sustainable anti-cancer therapy agents, and the fusion of biotechnology with AI-aided characterization offers considerable digital prospects for future cancer treatment solutions.

The novelty of our study lies in the utilization of PEGylated CL to encapsulate ZnO NPs and evaluate their impact on human cervical cancer cells (HeLa) and mouse fibroblast (L929) cells. This approach combines two biologically active substances with the potential to enhance anti-cancer properties. By encapsulating ZnO NPs in the PEGylated CL matrix, we aimed to enhance stability and bioavailability, potentially improving efficacy against cancer cells. Consequently, our study has profound implications for the advancement of sustainable nano-drug carriers in pharmaceutical nanotechnology.

Numerous methods have been developed to characterize organic/inorganic hybrid nanostructures using AI. For instance, machine learning algorithms and AI network approaches can be used to identify the significant surface properties of nanostructures, such as their shape, size, and morphology, in microscopy images of nanomaterials produced by methodologies such as TEM or SEM. AI characterization can also be used to model how nanomaterials behave under various settings, for example, when exposed to various compounds or extreme temperature changes, allowing the estimation of how they will interact with other materials or biological systems. This is essential for developing cutting-edge applications in energy, material science, and biomedicine. The potential for AI characterization is enormous, and may greatly accelerate the creation of new nanostructures and expand our understanding of their properties. We synthesized sustainable CL/ZnO NPs using a sonication method and characterized them using various techniques including XRD, FTIR, SEM, TEM, and AI-TEM. Furthermore, our investigation of the effects of CL/ZnO NPs on HeLa and L929 cells revealed that the NPs displayed significant cytotoxic activity against cancer cells with minimal toxicity to fibroblast cells. These findings suggest that the green synthesis of CL/ZnO NPs could be sustainable nano-drug carriers, highlighting the potential for developing innovative nanotherapeutics for cancer treatment and new complementary pharmaceutical products for cancer treatment. Nevertheless, confirmation of *in vitro* nano-drug carrier-based sustainability requires further clinical trials.

2. Materials and method

2.1. Materials

Matcha powder was purchased from Arifoğlu Company (Turkey). Zinc nitrate hexahydrate ($Zn(NO_3)_2{\cdot}6H_2O$), sodium hydroxide (NaOH), and MF-Millipore membrane filters were purchased from Merck Company (Germany). Polyethylene glycol 400 (PEG 400) was purchased from Sigma-Aldrich Company (Germany). Ultrapure water was provided by a Human Ultra-Pure Water System

(water resistance: 18.3 Mohm) and was used for the preparation of all NPs.

2.2. Synthesis of CL/ZnO NPs

The synthesis of CL/ZnO NPs involved several steps. First, 5 g of the matcha powder was dissolved in 100 ml of pure deionized water using a magnetic stirrer for 10 min at 25°C. The solution was maintained in the dark at room temperature for 48 hours. In the second step, a solution of 0.1 M $Zn(NO_3)_2{\cdot}6H_2O$, and 0.2 M NaOH was prepared in deionized pure water. In the third step, 0.5 mL of PEG400 and $Zn(NO_3)_2{\cdot}6H_2O$ solution was added to the CL solution, followed by NaOH solution dropwise added at 30% amplitude under a sonicator at 25°C for 30 min. Afterwards, the mixture was filtered first through a 0.45 μm pore size membrane filter and then through a 0.22 μm pore size membrane filter to remove any impurities and it was dried in a vacuum oven at 80°C. Finally, CL/ZnO NPs were stored at 25°C in a sterile container for further analysis.

2.3. Characterization of CL/ZnO NPs

The synthesized CL/ZnO NPs were characterized using specific techniques to evaluate their structural and chemical properties. The following characterization techniques were employed:

The crystalline structure of the CL/ZnO NPs was determined using an XRD (Rigaku MiniFlex XRD) equip ped with Cu Kα radiation ($\lambda = 1.5460$ Å) operating at 30 kV and 100 mA (wide range of 5-90°, scanning speed of 8°/min and step of 0.01°). The functional groups and chemical bonds in the CL/ZnO NPs were investigated using a FTIR (Perkin Elmer Spectrum Two). The analysis was performed in the frequency range – 400–4000 cm^{-1} with a resolution of 4 cm^{-1} and eight scans to obtain detailed information about the molecular vibrations and chemical composition of the CL/ZnO NPs. The UV–Visible absorbance spectrum of CL/ZnO NPs was measured using a UV–Visible spectrophotometer (Shimadzu UV-2600) across the wavelength range of 200–800 nm. The surface morphology and particle size distribution of the CL/ZnO NPs were examined by SEM (FEI QUANTA 450). Prior to imaging, the CL/ZnO NPs were coated with a thin conductive layer (double-coated with gold) to enhance their conductivity. SEM imaging provided high-resolution images and valuable insights into surface properties and particle size characteristics. The structure, size, and shape of the CL/ZnO NPs were observed using a transmission electron microscope (Hitachi, HighTech HT7700) operating at 100 kV in the high vacuum mode. Thin samples of the CL/ZnO NPs were prepared by dispersing them in a suitable solvent (deionized pure water) and depositing a drop onto a TEM grid. TEM analysis allowed for the visualization of individual CL/ZnO NPs and provided detailed information regarding their structural properties. Moreover, the TEM images of the CL/ZnO NPs underwent a preparatory analysis utilizing advanced AI-driven methodologies, primarily executed through Python's powerful libraries. This initial phase involved image processing techniques, including normalization and thresholding with OpenCV, feature extraction through TensorFlow Keras' deep learning models, and detailed texture analysis facilitated by Scikit-image. These AI-enhanced pre-processing steps were crucial for increasing the images' clarity and detail, thereby enabling better examination of NPs characteristics. Subsequently, the pre-processed images were analyzed using the ImageJ software. While ImageJ itself is not inherently an AI software, it serves as an invaluable platform for the quantitative analysis of particle size distribution, shape, and structural properties in AI-optimized images. The combination of Python's AI-driven image enhancement with ImageJ's comprehensive analysis capabilities underscores our innovative approach of blending cutting-edge computational techniques with robust, established imaging software to achieve unprecedented precision and efficiency in NPs surface analysis.

In this study, we used a combination of advanced computer vision techniques and texture analysis to explore the characteristics of CL/ZnO NPs in the TEM images. This approach, encompassing edge detection, contrast enhancement, and texture property assessment, provides a comprehensive understanding of NPs morphology and distribution within the sample. The TEM image was loaded in the color mode using OpenCV, a powerful library for image processing in Python. The Canny edge detection algorithm was applied to the image to delineate NP boundaries [57]. This method is highly effective in highlighting the subtle edges of small particles, which is essential for an accurate particle size and shape analysis. The image was converted to grayscale to facilitate texture analysis using a Gray-Level Co-occurrence Matrix (GLCM) [58]. The GLCM is a statistical method for examining the texture of an image by calculating the frequency with which pairs of pixels with specific values and in a specified spatial relationship occur in the image. This method provides a variety of textural features.

- Contrast measures local variations in the gray-level co-occurrence matrix.
- Dissimilarity: This quantifies texture variations bet ween a pixel and its neighbor over the entire image.
- Homogeneity: Assess the closeness of the distribution of elements in the GLCM to the diagonal.

2.4. Cytotoxicity assay

The human cervical cancer cell line HeLa (ATCC® CCL-2™) and mouse fibroblast cell line L929 (ATCC CCL-1)

were obtained from the American Type Culture Collection (ATCC, Manassas, Virginia, USA). HeLa and L929 cells used in the experiments were derived from passage numbers P5-P10. Both cell lines were cultured at 37°C in 5% CO_2 in Dulbecco's modified Eagle's medium (DMEM; Sigma-Aldrich, USA) supplemented with 10% Fetal Bovine Serum (FBS) (Gibco, USA), 100 U/mL penicillin, and 100 μg/mL streptomycin (Multicell, Wisent Bioproducts, Canada). To assess the *in vitro* toxicity of CL and CL/ZnO NPs, 100 μL of cell suspension containing 1×10^4 cells/well was seeded into 96-well cell culture plates and incubated overnight at 37°C in 5% CO_2. Prior to each experiment, the number of viable cells was determined using a Cedex XS Cell Counter (Innovatis, Roche, Germany). Serial twofold dilutions of CL and CL/ZnO NPs (ranging from 100 to 2.5 μg mL^{-1}) were prepared, and 100 μL of each sample was added in triplicate to the wells and incubated for 24 and 48 hours. After the incubation period, 10 μL of MTT (3-(4,5-dimethyl thiazolyl-2)−2,5-diphenyltetrazolium bromide) solution (ABCR, Germany) was added to each well and incubated at 37°C in a 5% CO_2 incubator for 4 h. Next, the contents of the wells were removed and 100 μL of dimethyl sulfoxide (DMSO) was added to each well to solubilize the formazan crystals. The absorbance of each well was measured at a wavelength of 595 nm using a microplate reader (FilterMax F5; Molecular Devices, USA). Cells that were not treated with CL or with CL/ZnO NP were used as controls (untreated negative control) and considered 100% viable. The following equation (Eq. 1) was used to determine the cytotoxic effects of CL and CL/ZnO NPs [59].

$$\begin{aligned}&\text{Cytotoxicity}(\%)\\&= [(\text{Mean ODcontrol} - \text{Mean ODtreated})/\\&\quad \text{Mean ODcontrol}] \times 100 \qquad (1)\end{aligned}$$

The half-maximal inhibitory concentration (IC_{50}) was calculated using Calcusyn software.

2.5. Hoechst staining

Morphological changes in HeLa cells were observed after 48 hours of treatment with CL or CL/ZnO NPs by confocal microscopy (Leica, Wetzlar, Germany). Fluorescence images were obtained using a Leica DMI 4000 B inverted microscope equipped with a spectral TCS SPE confocal microscope (Leica). To perform this experiment, cells were seeded on clean coverslips at a concentration of 1×10^5 cells/mL in a 6-well plate and incubated for 24 hours. Once the cells were attached, they were treated with the IC_{50} concentrations of CL and CL/ZnO NPs for 48 hours. Cells were fixed with 4% paraformaldehyde for 20 minutes and washed twice with phosphate-buffered saline (PBS). Afterwards, the cells were stained with Hoechst 33342 (Sigma Aldrich Company, USA) at a concentration of 0.1 μg mL^{-1} for 10 minutes and washed with PBS. Glass coverslips were removed from the wells and left to dry at room temperature. After mounting, the coverslips were observed under a confocal microscope, and images were captured using Leica imaging.

3. Results and discussion

3.1. Characterization

The characterization techniques mentioned above (XRD, FTIR, UV, SEM, TEM, and AI-TEM) were employed to obtain comprehensive information on the synthesized CL/ZnO NPs. These techniques have been used to determine crystal structure, composition, surface morphology, particle size, and other physical properties.

The XRD graph of the prepared CL/ZnO NPs revealed distinct diffraction peaks corresponding to specific crystal planes (Figure 1). According to the XRD results, the diffraction pattern displayed well-defined peaks at various angles, indicating the presence of crystalline phases in the nanostructure. The CL/ZnO NPs diffraction peaks were observed at 32.13°, 34.77°, 36.64°, 47.92°, 56.96°, 63.21°, 66.77°, 68.29°, 69.43 °, 72.97°, 77.32°, and 81.71°, which were associated with the crystalline planes of Miller indices (100), (002), (101), (102), (110), (103), (200), (112), (201), (004), and (202), respectively (JCPDS database 01-075-1526). Furthermore, the XRD analysis confirmed that the prepared CL/ZnO NPs comprised a hexagonal wurtzite ZnO phase. By applying Scherrer's Equation ($D = 0.9/\beta\cos\theta$, where β represents the Full Width at Half Maximum (FWHM), θ denotes the angle of diffraction, and λ is the wavelength) and considering the space group P63mc and lattice parameters (a = b: 2.801 Å and c: 5.149 Å), the average crystallite size of ZnO contained in the synthesized CL/ZnO NPs was determined to be 95 nm. The lattice parameters and crystallographic orientation of the CL/ZnO NPs may be determined from the positions and intensities of the diffraction peaks, which assists in identifying their structural characteristics. The agreement between the XRD results and those reported by Alamdari et al. [60] confirms the successful synthesis of ZnO NPs. This consistency contributes to the growing knowledge of green synthesis methods for organic/inorganic hybrid nanostructures and highlights the crystalline phases of the ZnO NPs.

In our previous study, we performed comprehensive FTIR analysis to investigate the molecular composition and functional groups of the extract [61]. Building on this knowledge, in the present study, we used the same extract for the synthesis of ZnO NPs. This approach allowed us to leverage the natural components present in the extract to produce powdered ZnO NPs in an environment-friendly manner. The FTIR spectra of CL and CL/ZnO NPs are shown in Figure

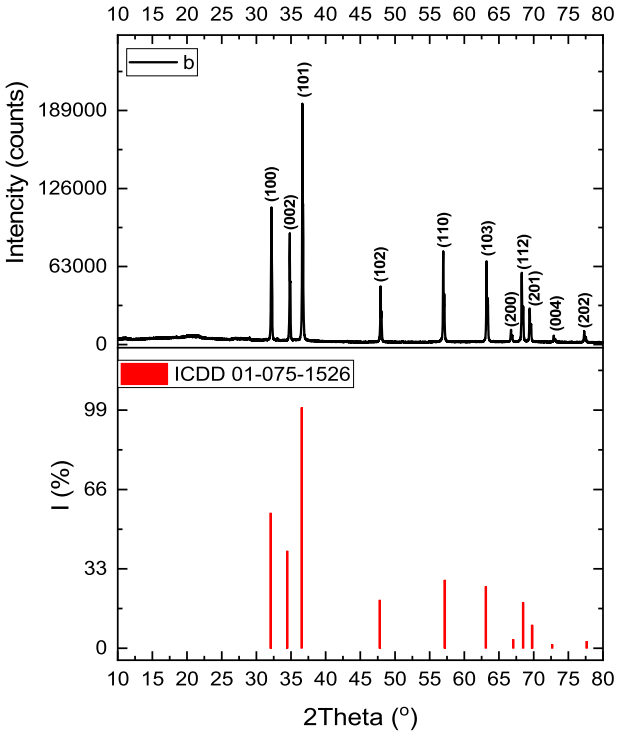

Figure 1. XRD pattern of the CL/ZnO NPs.

2(a,b). The FTIR spectrum of CL showed characteristic peaks at 3283 cm^{-1} (–OH), 2979 cm^{-1} (asymmetric $-CH_2$), 1623 cm^{-1} (C = O stretching of polyphenols), 1512 cm^{-1} (flavonoids), 1448 cm^{-1} (–CH bending), 1371 cm^{-1} (–CH stretching), 1235 cm^{-1} (C–O–C stretching of ether), 1144 cm^{-1} (C–O stretching), and 1026 cm^{-1} (–CH in-plane bending) (Figure 2(a)) [61]. These peaks provide insights into the presence of specific functional groups and molecular structures within the extract, such as hydroxyl, methylene, carbonyl, flavonoid, and –CH groups. The FTIR spectrum of CL/ZnO NPs showed distinct characteristic peaks, indicative of their chemical composition and molecular structure. The peak observed at 3283 cm^{-1} corresponds to the stretching vibration of hydroxyl (–OH) groups, indicating the presence of these functional groups within the structure. The peaks at 2921 and 2846 cm^{-1} represent the asymmetric and symmetric stretching vibrations of the methylene (– CH_2) groups, respectively, providing information about the structural arrangement of these groups in the nanostructure. Additionally, the peak observed at 1625 cm^{-1} indicated the stretching vibration of the carbonyl (C = O) groups present in the NPs, highlighting the presence of these specific constituents. The peak at 1517 cm^{-1} suggested the presence of flavonoids, which contributed to the overall chemical composition of the nanostructures. Furthermore, the peaks at 1449 and 1371 cm^{-1} correspond to the bending and stretching vibrations, respectively, of specific –CH and gem-dimethyl (–CH) groups, providing insight into the molecular arrangement and connectivity of these groups in the structure. The peaks observed at 1231 and 1145 cm^{-1} indicate the stretching vibrations of carbon–oxygen (C–O) and ether (C–O–C) groups, respectively, providing information about the presence and connectivity of these functional groups in the nanostructure. Finally, the peak observed at 1017 cm^{-1} corresponded to the in-plane bending vibration of the CH groups, revealing the structural arrangement and bonding characteristics of these groups within the structure. The peak observed around 510-600 cm^{-1} in the FTIR analysis of CL/ZnO NPs can be attributed to the bending vibrations of Zn-O bonds, providing further evidence for the presence of these bonds in the nanostructure. Overall, FTIR analysis offers valuable information regarding the chemical constituents and molecular structure of CL/ZnO NPs, enabling a comprehensive understanding of their compositions and potential applications. Additionally, the optical bandgap (Eg) was determined utilizing the Tauc equation (Eq. 2) [62], involving the plot of $(\alpha h\upsilon)^2$ against the photon energy ($h\upsilon$), as depicted in Figure 2(c,d), where α and $h\upsilon$ represent the absorption coefficient and the photon energy, respectively.

$$\alpha h\upsilon^2 = k(h\upsilon - E_g) \quad (2)$$

The optical properties (log A, α, $h\nu$, and $(\alpha h\upsilon)^2$) were calculated to determine the bandgap energy of CL/ZnO NPs. The estimated Eg value for CL/ZnO NPs was determined to be 3.33 eV. The experimental results obtained are consistent with data reported for other ZnO NPs in the literature [63].

The SEM image, SEM-EDX mapping pattern of the element distribution (Zn and O) in the scanned area, and SEM-EDX analysis of CL/ZnO NPs were conducted to investigate the morphology of the CL/ZnO NPs (Figure 3a–d). Upon careful examination of the SEM micrograph, it was evident that it was difficult to distinguish the borders of certain ZnO NPs (Figure 3a). This can be attributed to the presence of a matrix shell composed of CL surrounding the ZnO NPs. The unique properties of this matrix shell play a significant role in explaining the indistinct NPs boundaries observed in the SEM images. The PEGlayted CL matrix increases the surface area of CL/ZnO NPs, preventing them from aggregating or agglomerating over time. The PEGlayted CL matrix shell, acting as a bridging medium, facilitates the homogeneous distribution of NPs. Consequently, the individual CL/ZnO NPs borders were more challenging to discern in the SEM images. In line with the EDX spectrum of the CL/ZnO NPs, the obtained peaks in the spectrum corresponded to Zn and O (Figure 3d). The weight percentages derived from the analysis indicated that Zn and O accounted for 80.34% and 19.66% of the CL/ZnO NPs, respectively. In summary, SEM and SEM-EDX analysis revealed the presence of a bio-tea extract matrix shell surrounding the CL/ZnO NPs, which led to difficulties in distinguishing individual CL/ZnO NPs boundaries in

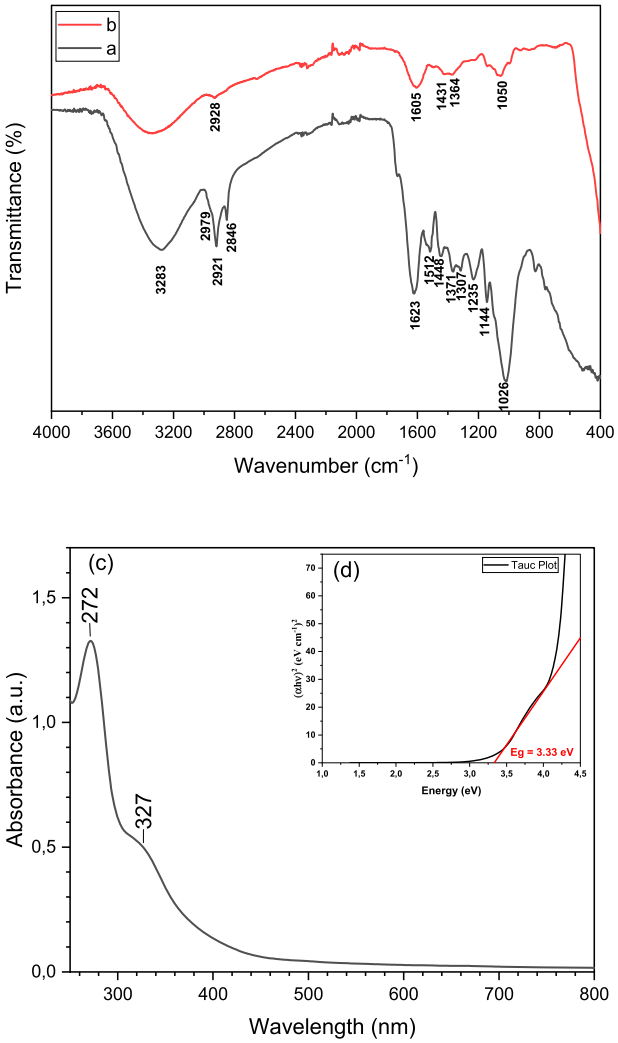

Figure 2. FTIR graphs of (a) CL and (b) CL/ZnO NPs, (c) UV – Vis absorption spectra, and (d) Tauc plot of the CL/ZnO NPs.

the SEM images. Weight percentage analysis confirmed the presence of Zn and O in the CL/ZnO NPs. Additionally, NaOH played a crucial role in the sonosynthesis process by adjusting the pH, promoting the precipitation of Zn ions, and facilitating the formation of ZnO NPs, thereby contributing to the control of particle size and morphology. This sonoprocess is elucidated by the following Eqs. (2-5) [64,65]:

$$Zn^{2+} + 2OH^- \overset{\text{ultrasound waves}}{\longleftrightarrow} Zn(OH)_2 \quad (3)$$

$$Zn(OH)_2 + 2OH^- \longleftrightarrow [Zn(OH)_4]^2 \quad (4)$$

$$[Zn(OH)_4]^{2-} + 2OH^- \longleftrightarrow ZnO_2^{2-} + 2H_2O \quad (5)$$

$$ZnO_2^{2-} + H_2O \longleftrightarrow ZnO + 2OH^- \quad (6)$$

In Figure 4, the study of CL/ZnO NPs involved various imaging techniques, including (a) traditional TEM, (b) AI-supported TEM images in threshold mode-8 bit, (c) AI-supported TEM images in Red Blue Green (RGB) mode-8 bit, (d) AI-supported surface plot, (e) RGB color histogram of the CL/ZnO NPs, and (f) AI-enhanced TEM images of CL/ZnO NPs showing detailed surface characteristics and texture analysis results, which were used to carefully analyze the morphology of CL/ZnO NPs.

In the characterization of CL/ZnO NPs using Transmission Electron Microscopy (TEM), we employed a suite of advanced computational techniques to augment traditional image analysis methods. This approach was driven by the necessity to extract detailed morphological and textural information from the TEM images, which are crucial for understanding the NPs' interactions with biological systems. To achieve this, we utilized several Python libraries that are known for their robust capabilities in image processing and analysis.

- **OpenCV (cv2)**: A foundational library for image processing tasks, including image normalization, thresholding, and contour detection. OpenCV facilitated the initial processing of TEM images, preparing them for further analysis.
- **TensorFlow Keras with the VGG16 model**: Leveraged for deep learning-based feature extraction. This pre-trained neural network model was instrumental in identifying and quantifying intricate features within the NPs, offering insights beyond conventional analysis methods.
- **Scikit-image (skimage)**: Used for a broad spectrum of image processing tasks, supporting the enhancement and quantification of image features. This library complemented our analysis by facilitating texture analysis and edge detection.

This AI-modified surface characterization enabled better visualization and differentiation of the different structures and features of CL/ZnO NPs. The surface properties of the NPs were determined using a surface plot and 3D visualization approach. The AI support of this method probably assisted in precisely evaluating and displaying the surface data, thereby providing important insights into the topography of CL/ZnO NPs. RGB color channels were used to describe the distribution of colors in a picture using the RGB color histogram. The color distribution and intensity changes of CL/ZnO NPs can be used to infer certain NP characteristics or attributes by analyzing the RGB color histogram of these particles. Researchers have thoroughly analyzed and understood the structural and optical characteristics of NPs using these imaging techniques, providing new insights into their prospective applications in a variety of disciplines, including nanotechnology, materials science, and biological research [64–66]. Figure 4(a–e) provide valuable insights into the surface characteristics of the CL/ZnO NPs, offer significant information for further analysis and understanding. TEM images revealed the ZnO NPs in high-resolution detail,

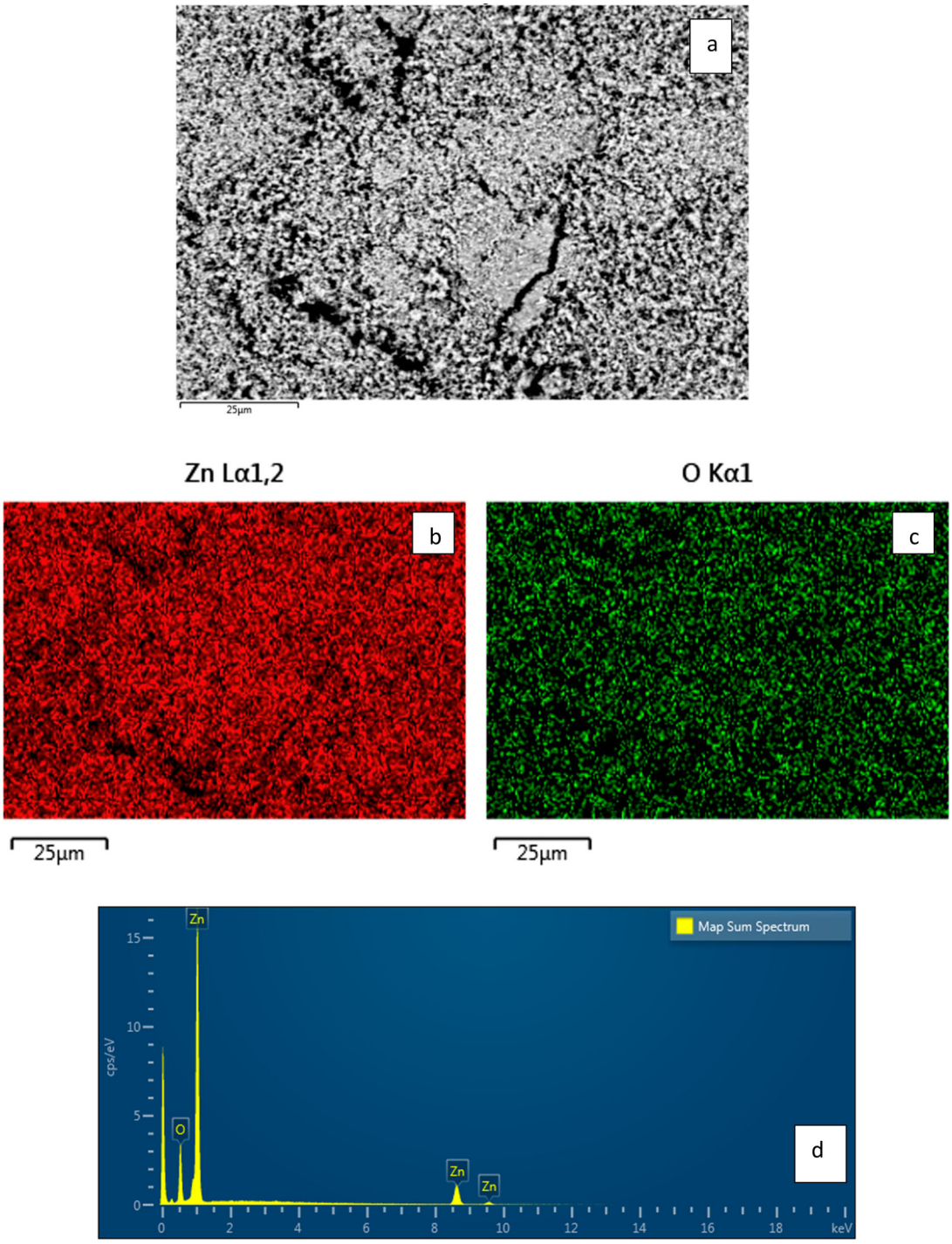

Figure 3. (a) SEM image, SEM-EDX mapping pattern of the element distribution: (b) Zn and (c) O in the scanned area, and (d) SEM-EDX analysis of CL/ZnO NPs.

highlighting their well-defined spherical shape. Additionally, the utilization of AI algorithms in image processing and analysis enhances our understanding of the CL/ZnO NPs. The AI-supported TEM image of the ZnO NPs provides further insight into the nanostructure, aiding in more precise and effective characterization of their surface characteristics. This cutting-edge approach improved our understanding of the spherical shape and well-defined morphology of ZnO NPs. Furthermore, the observed small particle size, averaging 40 ± 5 nm, indicates a synthesis process that led to the formation of highly homogeneous organic/inorganic hybrid nanostructures as CL/ZnO NPs. This small size indicates the effectiveness of the employed synthesis method, which allows the production of ZnO NPs with excellent surface characteristics.

After the texture analysis, image preprocessing was performed by applying Gaussian blur for noise reduction, which is crucial for minimizing false edges and enhancing the real features in the TEM images. Contrast enhancement was achieved through histogram equalization, a technique that improves the contrast in an image by stretching the range of intensity values. This technique converts a contrast-enhanced image

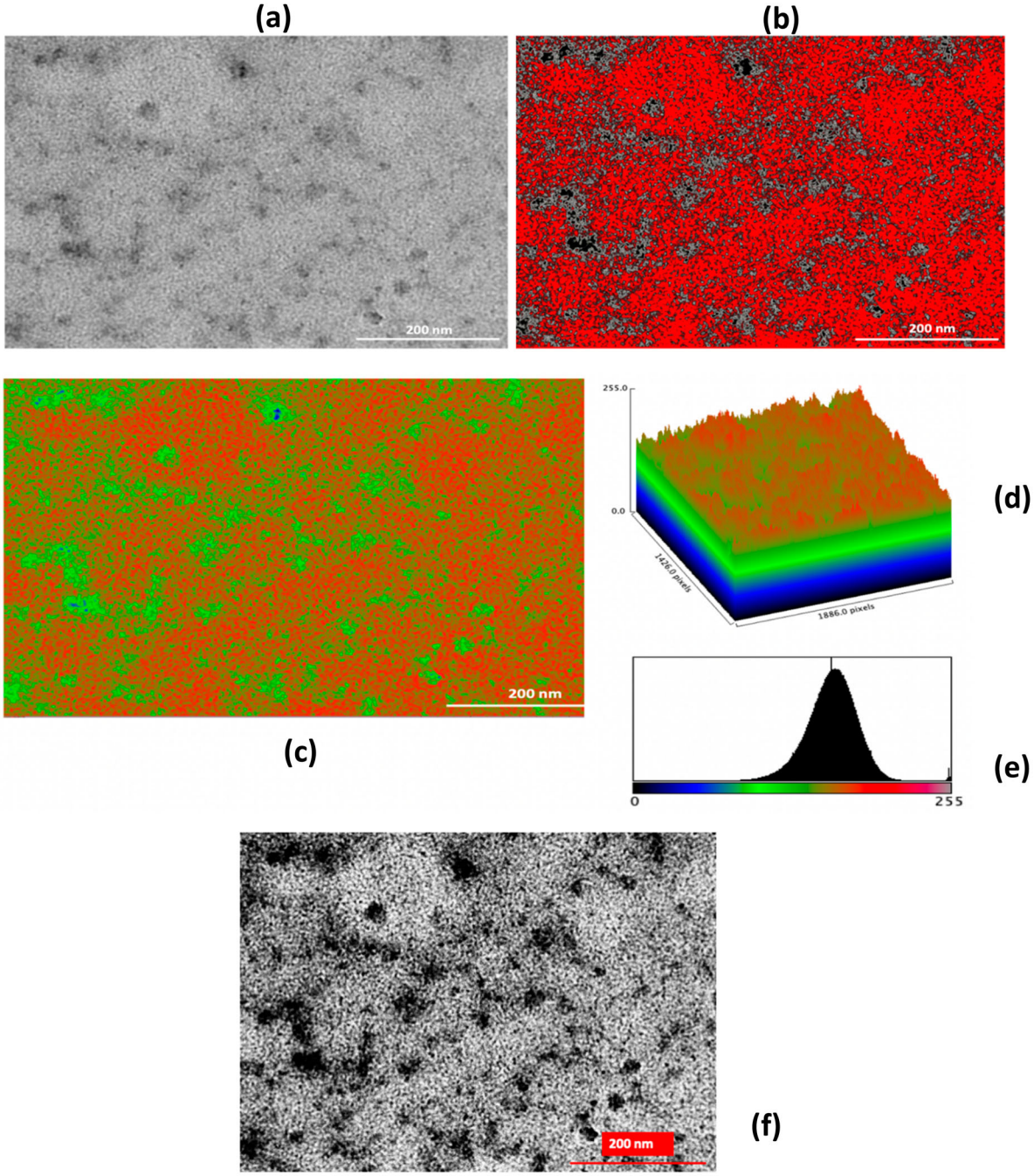

Figure 4. (a) TEM, (b) AI-supported TEM images (threshold mode-8 bit), (c) AI-supported TEM images (RGB mode-8 bit), (d) AI-supported surface plot, (e) RGB color histogram of the CL/ZnO NPs, and (f) AI-enhanced TEM Image of CL/ZnO NPs showcasing detailed surface characteristics and texture analysis results.

into a binary one. This process isolates NPs from the background, making it easier to analyze their distribution and morphology. The processed images (original, contrast-enhanced, and thresholded) were visualized and saved. This provides a valuable reference for comparative analysis and documentation. Figure 4(f) shows the results of the Canny edge detector, which revealed the precise boundaries of the NPs and provided a clear demarcation for further morphological analysis. Texture analysis results from the Gray-Level Co-occurrence Matrix (GLCM) of the TEM image revealed a contrast value of 719.77. This high value suggests significant local variation in the gray-level co-occurrence matrix. The TEM image indicates a substantial degree of variability in the intensity values across the surface of the NPs. High contrast values are typically associated with images that have a high level of detail and clearly defined edges, which are crucial for differentiating between different NP structures. The dissimilarity value for the enhanced image was 20.83. This value quantifies the variation in gray-level values between a pixel and its neighboring pixels across the entire image. This dissimilarity value implies that there is considerable textural irregularity within the NPs aggregation. This metric is particularly useful for assessing the heterogeneity of the physical makeup of the NPs. The

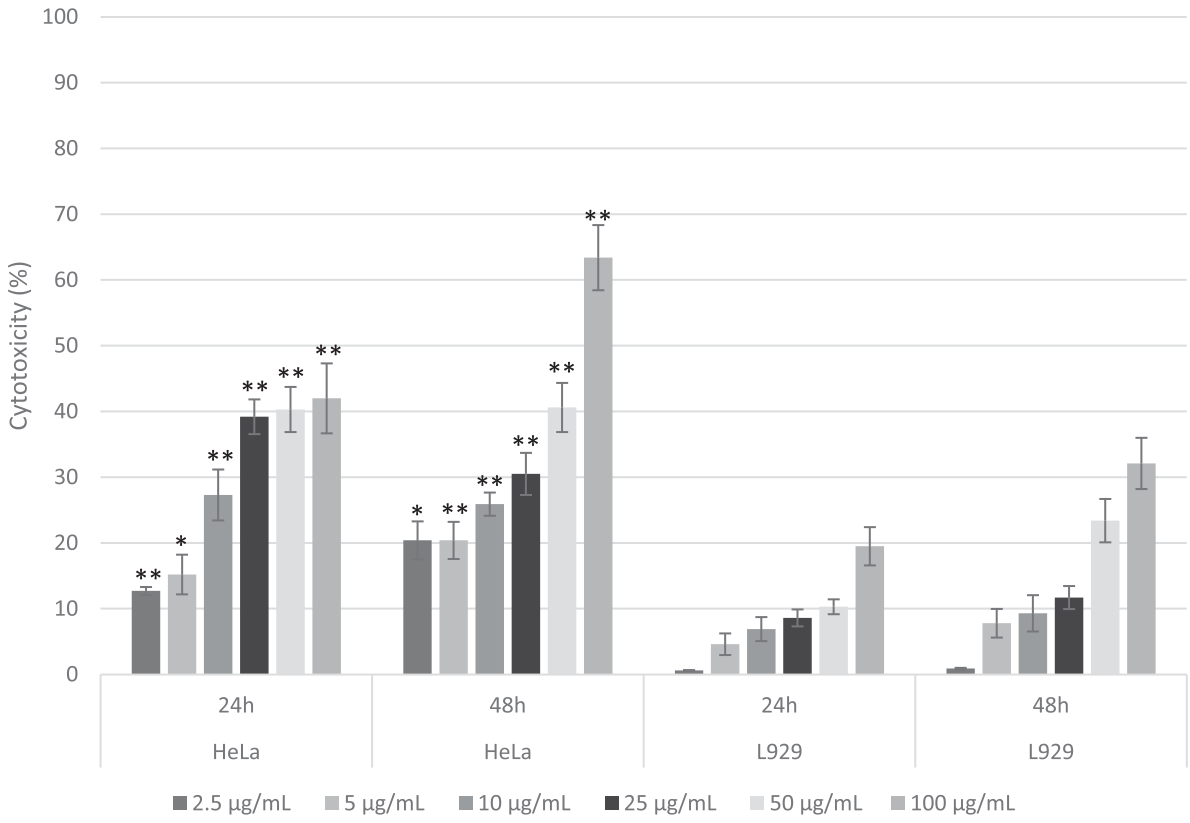

Figure 5. Dose – and time-dependent cytotoxic effects of CL on HeLa (cervical cancer) and comparison with L929 (Fibroblast) cells serving as controls, after 24 and 48 hours of treatment. The cytotoxicity was assessed using the MTT assay, with results expressed as percentages relative to untreated controls. Data are presented as mean ± standard error (SE) based on three independent experiments conducted in triplicate. Bars within cell types displaying asterisks denote significant differences determined by Welch's t-test ($*p \leq 0.05$, $**p \leq 0.01$).

homogeneity of the images is 0.07. A lower homogeneity value indicates less uniformity in the gray-level spatial distribution. In our TEM image, this suggests that the NPs and the matrix they were embedded in do not have a uniform texture. This could be indicative of the varying material compositions or phases within the sample. These texture parameters provide a comprehensive quantitative description of the NPs surfaces, offering a deeper understanding of their morphological characteristics. When combined with other image processing techniques and AI algorithms used in this study, these metrics contribute significantly to a more nuanced understanding of NPs, aiding the development of applications where surface properties are critical.

3.2. Cytotoxicity assay

In this study, CL and CL/ZnO NPs were used to assess their cytotoxicity in HeLa and L929 cells. Standard cytotoxicity assays, including MTT, were used to quantify cell viability and provide a reliable measure of the effects of the NPs. The cell viability was evaluated at different concentrations (2.5, 5, 10, 25, 50, and 100 µg/mL) for 24 and 48 hours. Figures 5 and 6 show the cytotoxic effects of CL and CL/ZnO NPs, respectively, on HeLa and L929 cells over two time periods at various concentrations. As shown in Figure 5 and Figure 6, cytotoxicity increased in both cell lines with increasing concentrations of CL and CL/ZnO NPs. After 48 hours of treatment, the IC_{50} values of CL and CL/ZnO NPs in HeLa cells were found to be 73.556 µg mL^{-1} and 13.708 µg mL^{-1}, respectively; the is as compared of L929 cells $IC_{50} > 100$ µg mL^{-1} and 91.986 µg mL^{-1}, respectively. Previously, the cytotoxicity of ZnO NPs against HeLa cells has been reported [67], corroborating our findings. Thomas et al. observed decreased viability of cancerous cells in a dose –and time-dependent manner, with an IC_{50} value of 31.6 µg mL^{-1} by ZnO NPs prepared from *Solanum nigrum* methanolic extract [67]. Similarly, Naiel et al. reported dose-dependent cytotoxicity of bio-synthesized ZnO NPs using an aqueous extract of sea lavender, *Limonium pruinosum* (L.) Chaz., which showed higher toxicity towards cancer cells than towards normal cells [68]. Ilangovan et al. reported that sustainable synthesis of ZnO NPs using aqueous extract of *Tagetes erecta* flower decreased the 50% cell viability of Hela cells at 26.53 µg mL^{-1} [69]. In the present study, CL/ZnO NPs showed higher toxicity towards cancer (HeLa) cells than towards normal (L929) cells. Our findings agree with those of several previous studies, which have shown that synthesized ZnO NPs showed higher cytotoxicity towards cancer cells [70,71]. For instance, Shivyari et al. (2022) observed that ZnO NPs synthesized using *Artemisia*

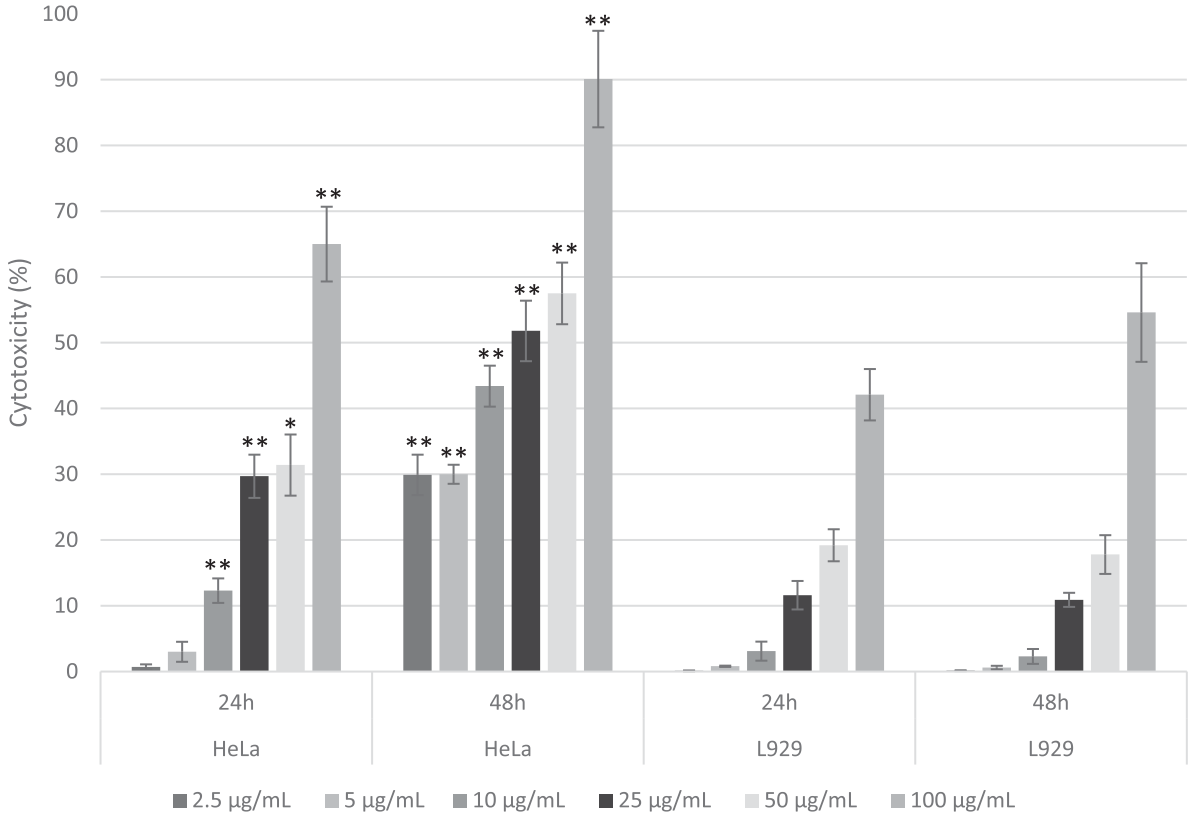

Figure 6. Dose – and time-dependent cytotoxic effects of CL/ZnO nanoparticles on HeLa (cervical cancer) and L929 (fibroblast) cells after 24 and 48 hours of treatment. Cytotoxicity was assessed using the MTT assay, with results expressed as percentages relative to untreated controls. Data are presented as mean ± standard error (SE) from three independent experiments, each conducted in triplicate. Statistical significance was determined using Welch's t-test, with bars indicating significant differences within cell types denoted by asterisks ($*p \leq 0.05$, $**p \leq 0.01$).

Table 1. ANOVA results for the effects of CL and CL/ZnO NPs on cell viability in HeLa and L929 cells: concentration and duration analysis.

	HeLa Cells		L929 Cells	
	Concentration effect	Duration effect	Concentration effect	Duration effect
CL	$F = 31.95, p < 0.0001$	$F = 4.10, p = 0.0523$	$F = 38.62, p < 0.0001$	$F = 24.83, p < 0.0001$
CL/ZnO NPs	$F = 207.04, p < 0.0001$	$F = 413.78, p < 0.0001$	$F = 145.56, p < 0.0001$	$F = 1.58, p = 0.2183$

scoparia extract had much less effect on normal human foreskin fibroblast (HFF) cells against Huh-7 liver cancer cells [72]. Another study reported that synthesized ZnO NPs from *Nilgirius ciliatus* were found to be cytotoxic towards MCF-7 cancer cells but nontoxic towards normal L929 fibroblast cell lines [73].

A comparative analysis of the cytotoxicity of CL and CL/ZnO NPs in HeLa and L929 cells was performed using ANOVA. Figure 7 illustrates the comparative analysis of the cytotoxic effects of CL and CL/ZnO NPs on L929 (fibroblasts) and HeLa (cervical cancer) cells at various concentrations.

The ANOVA results provided insights into the statistical significance of the effects of CL and CL/ZnO NPs on the viability of HeLa and L929 cells, considering different concentrations and durations (Table 1).

To assess the effects of CL and CL/ZnO NPs on HeLa and L929 cells, the effects of concentration and duration were examined. For CL in HeLa cells, a highly significant concentration effect ($F = 31.95$, $p < 0.0001$) indicated substantial differences in cell viability across concentrations, whereas the duration effect was marginally significant ($F = 4.10, p = 0.0523$), suggesting a less pronounced but notable difference between 24 and 48 hours. Similarly, CL on L929 cells exhibited highly significant effects for both concentration ($F = 38.62$, $p < 0.0001$) and duration ($F = 24.83$, $p < 0.0001$), emphasizing substantial differences in cell viability across concentrations and between the two durations. In contrast, CL/ZnO NPs showed highly significant concentration effects on both HeLa ($F = 207.04$, $p < 0.0001$) and L929 ($F = 145.56$, $p < 0.0001$) cells, indicating significant differences in cell viability at various concentrations. The duration effect of CL/ZnO NPs on HeLa cells was highly significant ($F = 413.78$, $p < 0.0001$), highlighting a notable difference between 24 and 48 hours. Surprisingly, the duration effect of CL/ZnO NPs on L929 cells was not significant ($F = 1.58$,

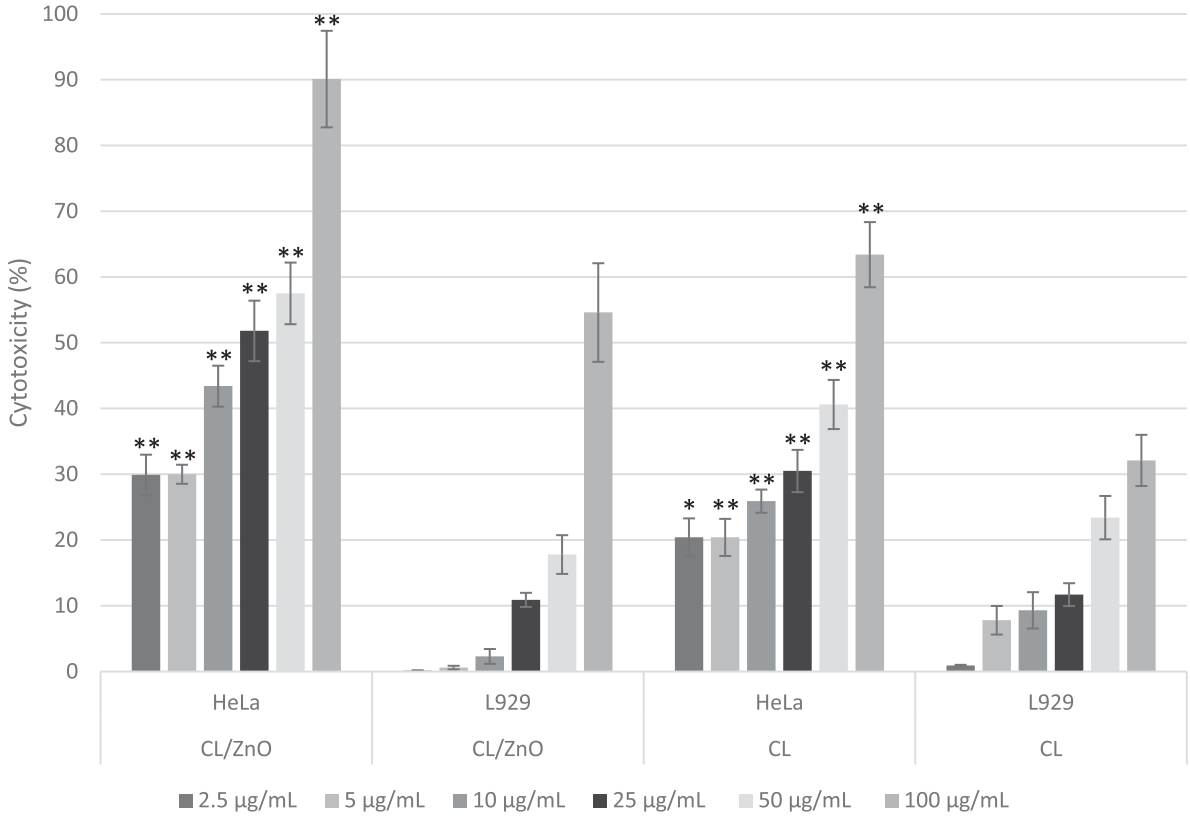

Figure 7. Comparative analysis of the cytotoxic effects of CL/ZnO nanoparticles and CL on HeLa (cervical cancer) and L929 (fibroblast) cells after 48 hours of treatment. Cytotoxicity was quantified as percentages relative to untreated controls. Data are represented as mean ± standard error (SE) from three independent experiments, each conducted in triplicate. Comparative analyses were performed with Welch's t-test. Statistically significant differences within cell types are indicated by asterisks, with $*p \leq 0.05$ and $p \leq 0.01$ denoting levels of significance.

$p = 0.2183$), suggesting that the duration did not significantly affect the cell viability. These findings underscore the distinct responses of HeLa and L929 cells to CL and CL/ZnO NPs, in terms of concentration and duration.

These results suggest that both CL and CL/ZnO NPs exhibited a marked decrease in cell viability with increasing concentrations. This trend was evident in both cell lines, although it was more pronounced in HeLa cells, suggesting heightened sensitivity of cancer cells to NPs-induced cytotoxicity. A significant increase in the cytotoxicity was observed at 48 hours compared with 24 hours at all concentrations. This indicates that NPs exert a cumulative effect over time, potentially enhancing their therapeutic efficacy. Although both the nanostructures demonstrated considerable cytotoxicity, subtle variations were observed. CL/ZnO NPs encapsulated in CL showed slightly enhanced efficacy, particularly at higher concentrations and longer exposure times. This enhancement can be attributed to the synergistic effect of the bioactive compounds in the CL extract. Notably, the cytotoxic effects were more pronounced in HeLa cells than in L929 cells. This differential cytotoxicity underscores the potential selectivity of these NPs towards cancer cells, which is a desirable trait in cancer therapeutics to minimize harm to healthy tissues.

3.3. Hoechst staining

The cytotoxic effect of CL/ZnO NPs was confirmed by microscopic examination of the changes in the morphology of HeLa cells using Hoechst 33342 staining under a confocal microscope (Leica TCS SPE DMI4000B Confocal Microscope). When compared to CL, HeLa cells treated with IC_{50} concentration of CL/ZnO NPs showed morphological changes such as shrinkage, distorted shape, membrane blebbing, granulation, and vacuolization in the cytoplasm as an indicator of cytotoxicity after 48 hours (Figure 8a–c).

The cytotoxicity studies revealed that CL/ZnO NPs were more effective than CL at inhibiting the viability of HeLa cells. Numerous studies have shown that *Camellia sinensis* is a rich source of nutritional flavonoids such as epigallocatechin gallate and epigallocatechin [74,75]. Catechins have been reported to have anticancer effects, and many cell-based and animal studies have provided evidence to support the anti-cancer effects of catechins [76–78]. The mechanisms underlying the anti-cancer effect may be related to the induction of apoptosis, inhibition of tumor angiogenesis, antioxidant effects, and anti-inflammatory effects, which have been reported in many studies [78–81]. The greater cytotoxic effect of ZnO NPs can be attributed to numerous variables associated with their increased

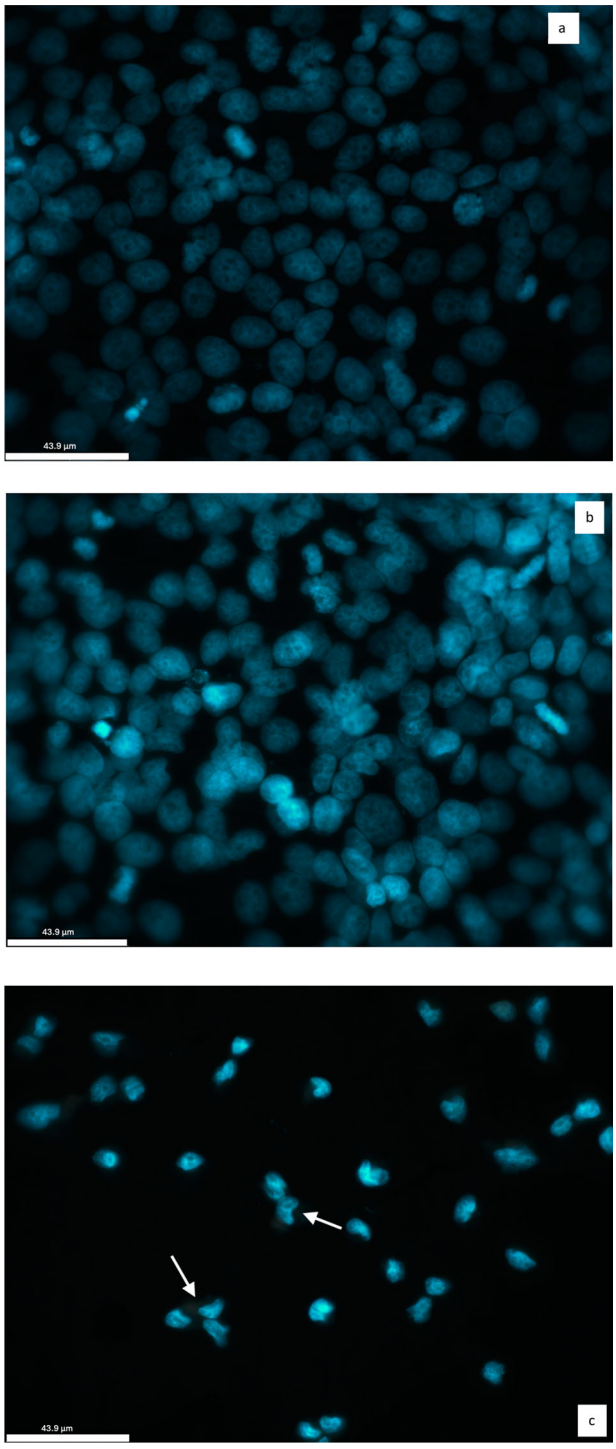

Figure 8. Representative confocal imaging of HeLa cells stained with Hoechst-33342. (a) HeLa cells in the absence of CL and CL/ZnO NPs (control) (b) HeLa cells treated with the IC_{50} concentration of CL for 48 hours (c) HeLa cells treated with the IC_{50} concentration of CL/ZnO NPs for 48 hours. The morphology of HeLa cells showing the cytotoxic effect of CL/ZnO NPs. The white arrows denote small or fragmented nuclei and shrunken cytoplasm (43.9 µm).

surface area and small particle size. A greater number of reactive sites, higher adsorption capacity, and improved cell penetration are factors that lead to the increased toxicity observed for smaller ZnO NPs [82]. Another possible mechanism of the cytotoxic effect of CL/ZnO NPs may result from the generation of higher amounts of ROS via apoptosis due to the photo-activation of ZnO NPs and the release of Zn ions from the NPs into the cell culture, which effectively influences cancer cells by disrupting their cell surface and protein leakage [83–85]. These results underscore the encouraging potential of CL and CL/ZnO NPs for cancer therapy. The dose-dependent and time-dependent cytotoxic effects, combined with their specificity towards cancer cells, establish these nanostructures as promising contenders for targeted cancer treatment. The incorporation of natural compounds into CL/ZnO NPs is important for enhancing their cytotoxic effects and potentially reducing side effects.

The comparative experimental findings presented in Table 2 provide a comprehensive overview of the surface properties of the ZnO NPs used in cancer research. Specifically, the table highlights significant changes in terms of shape and size, shedding light on the distinct morphological characteristics of these NPs in different experimental settings. In general, spherical ZnO NPs offer advantages such as large surface area, good cellular uptake, optimal drug loading capacity, superior targeting ability, and excellent biocompatibility, which potentially contribute to their efficacy in cancer treatment. However, it has been observed in various studies that the specific effects of ZnO-based nanostructures on cancer cells depend on the distinctive features of their morphology and the specific type of cancer cells targeted.

4. Conclusion

In this study, we successfully synthesized novel CL/ZnO NPs by using an economical and easily applicable sonication method and performed AI-assisted surface characterization. The Python libraries utilized in our work –OpenCV, TensorFlow Keras, and Scikit-image – played pivotal roles in uncovering nuanced details of CL/ZnO NPs. Remarkably, our investigations on cervical cancer cells (HeLa) and normal fibroblast cells (L929) demonstrated the significant cytotoxic activity of CL/ZnO NPs against cancer cells, while exhibiting minimal toxicity to normal cells. The present study has some limitations, such as the underlying molecular mechanisms of cytotoxicity or apoptosis, which have not been detailed. Further studies on the underlying mechanisms could advance our knowledge. This *in vitro* study underscores the potential of biosynthesized CL/ZnO NPs as organic/inorganic hybrid nano-drug carriers, offering fresh insights into the development of innovative nanotherapeutics and complementary pharmaceutical products for cancer treatment. Furthermore, these results highlight the potential of sonosynthesized CL/ZnO NPs as organic/inorganic hybrid nano-drug carriers, presenting viable solutions for the development of innovative nanotherapeutics and complementary pharmaceutical products for cancer treatment.

Table 2. A comprehensive overview of the surface properties of ZnO NPs in the context of cancer nano-based research.

Sample	Cancer cells	Surface properties	Ref.
Ag/ZnO nanostructures	HepG2 human liver cancer cells	rod-like structures with an average size of 22–58 nm	[86]
Au-decorated ZnO nanorods	MCF-7 human breast cancer cells	rod-like structures with average length and diameter of 84.4 nm and 11.7 nm	[87]
Manilkara littoralis leaf extract ZnO nanorods	MCF-7 human breast cancer cells	rod-like structures with size range of 50–200 nm.	[88]
Core-shell ZnO microspheres	HepG2 and MCF-7 cancer cells	spherical in shape with an average diameter of 19 nm.	[89]
Morinda tinctoria leaf extract-ZnO NPs	MCF-7 cancer cells	spherical in shape with an average diameter of 8–10 nm.	[71]
ZnO-curcumin nanocomposite	CHO–K1 cells and *in vivo* Swiss albino mice, C57BL/6	spherical structure with a diameter of 50 nm	[26]
CL/ZnO NPs	HeLa and L929 cells	spherical structure with a diameter of 40 ± 5 nm	This study

In the future, our work may lead to the development of more effective cancer treatment strategies in the field of nanomedicine. In conclusion, the present study demonstrated that spherical ZnO-based nanostructures exhibit favorable surface properties and structural characteristics when interacting with cancer cells, underscoring their significant potential in *in vitro* cancer research and future clinical investigations.

Disclosure statement

No potential conflict of interest was reported by the author(s).

Author contributions

AA: Conceptualization, formal analysis, investigation; FUA: biological formal analysis; IBK: biological formal analysis; TK: formal analysis; FO: surface formal analysis; SK: Writing – review and editing, supervision.

ORCID

Selcan Karakuş http://orcid.org/0000-0002-8368-4609

References

[1] Mohammadzadeh P, Ardestani MS, Mortazavi-Derazkola S, et al. PEG-Citrate dendrimer second generation: is this a good carrier for imaging agents In vitro and In vivo? IET Nanobiotechnol. 2019;13(6):560–564. doi: 10.1049/iet-nbt.2018.5360

[2] Hashemi Z, Mizwari ZM, Mohammadi-Aghdam S, et al. Sustainable green synthesis of silver nanoparticles using Sambucus ebulus phenolic extract (AgNPs@SEE): Optimization and assessment of photocatalytic degradation of methyl orange and their in vitro antibacterial and anticancer activity. Arab J Chem. 2022;15:103525. doi: 10.1016/j.arabjc.2021.103525

[3] Ebrahimzadeh MA, Hashemi Z, Mohammadyan M, et al. In vitro cytotoxicity against human cancer cell lines (MCF-7 and AGS), antileishmanial and antibacterial activities of green synthesized silver nanoparticles using Scrophularia striata extract. Surf Interfaces. 2021;23:100963. doi: 10.1016/j.surfin.2021.100963

[4] Khormali K, Mizwari ZM, Masoumeh Ghoreishi S, et al. Novel Dy2O3/ZnO-Au ternary nanocomposites: green synthesis using pomegranate fruit extract, characterization and their photocatalytic and antibacterial properties. Bioorg Chem. 2021;115:105204. doi: 10.1016/j.bioorg.2021.105204

[5] Hashemi Z, Shirzadi-Ahodashti M, Mortazavi-Derazkola S, et al. Sustainable biosynthesis of metallic silver nanoparticles using barberry phenolic extract: Optimization and evaluation of photocatalytic, in vitro cytotoxicity, and antibacterial activities against multidrug-resistant bacteria. Inorg Chem Commun. 2022;139:109320. doi: 10.1016/j.inoche.2022.109320

[6] Fouladi-Fard R, Aali R, Mohammadi-Aghdam S, et al. The surface modification of spherical ZnO with Ag nanoparticles: a novel agent, biogenic synthesis, catalytic and antibacterial activities. Arab J Chem. 2022;15:103658. doi: 10.1016/j.arabjc.2021.103658

[7] Shirzadi-Ahodashti M, Hashemi Z, Mortazavi Y, et al. Discovery of high antibacterial and catalytic activities against multi-drug resistant clinical bacteria and hazardous pollutants by biosynthesized of silver nanoparticles using Stachys inflata extract (AgNPs@SI). Colloids Surf A Physicochem Eng Asp. 2021;617:126383. doi: 10.1016/j.colsurfa.2021.126383

[8] Dutta D, Das BM. Scope of green nanotechnology towards amalgamation of green chemistry for cleaner environment: a review on synthesis and applications of green nanoparticles. Environ Nanotechnol Monit Manag. 2021;15:100418. doi: 10.1016/J.ENMM.2020.100418

[9] Liu D, Liu L, Yao L, et al. Synthesis of ZnO nanoparticles using radish root extract for effective wound dressing agents for diabetic foot ulcers in nursing care. J Drug Deliv Sci Technol. 2020;55:101364. doi: 10.1016/j.jddst.2019.101364

[10] Malathi S, Balashanmugam P, Devasena T, et al. Enhan ced antibacterial activity and wound healing by a novel collagen blended ZnO nanoparticles embedded niosome nanocomposites. J Drug Deliv Sci Technol. 2021;63:102498. doi: 10.1016/j.jddst.2021.102498

[11] Danışman-Kalındemirtaş F, Afşin Kariper İ, Erdemir G, et al. Evaluation of anticancer effects of carboplatin-gelatin nanoparticles in different sizes synthesized with newly self-assembly method by exposure to IR light. Sci Rep. 12(123AD):10686. doi: 10.1038/s41598-022-15051-7

[12] Rudramurthy GR, Swamy MK. Potential applications of engineered nanoparticles in medicine and biology: an update. J Biol Inorg Chem. 2018;23(8):1185–1204. doi: 10.1007/s00775-018-1600-6

[13] Khan ST, Ahmad J, Ahamed M, et al. Zinc oxide and titanium dioxide nanoparticles induce oxidative stress, inhibit growth, and attenuate biofilm formation activity of Streptococcus mitis. J Biol Inorg Chem. 2016;21(3):295–303. doi: 10.1007/s00775-016-1339-x

[14] Ahmad J, Wahab R, Siddiqui MA, et al. Cytotoxicity and cell death induced by engineered nanostructures (quantum dots and nanoparticles) in human cell lines. J Biol Inorg Chem. 2020;25(2):325–338. doi: 10.1007/s00775-020-01764-5
[15] Ansari MA, Mousa S, Asiri M, et al. Biofabricated fatty acids-capped silver nanoparticles as potential antibacterial, antifungal, antibiofilm and anticancer agents. Pharmaceuticals. 2021;14(2):139. doi: 10.3390/ph14020139
[16] Khan FA, Lammari N, Muhammad Siar AS, et al. Quantum dots encapsulated with curcumin inhibit the growth of colon cancer, breast cancer and bacterial cells. Nanomedicine (Lond). 2020;15(10):969–980. doi: 10.2217/nnm-2019-0429
[17] Khan FA, Akhtar S, Almofty SA, et al. FMSP-Nanoparticles induced cell death on human breast adenocarcinoma cell line (MCF-7 cells): morphometric analysis. Biomole cules. 2018;8(2):32. doi: 10.3390/BIOM8020032
[18] Thirupathi B, Pongen YL, Kaveriyappan GR, et al. Padina boergesenii mediated synthesis of Se-ZnO bimetallic nanoparticles for effective anticancer activity. Front Microbiol. 2024;15:1358467. doi: 10.3389/fmicb.2024.1358467
[19] Hamdani AM, Wani IA, Bhat NA. Sources, structure, properties and health benefits of plant gums: a review. Int J Biol Macromol. 2019;135:46–61. doi: 10.1016/j.ijbiomac.2019.05.103
[20] Li F, Qasim S, Li D, et al. Updated review on green tea polyphenol epigallocatechin-3-gallate as a cancer epigenetic regulator. Semin Cancer Biol. 2022;83:335–352. doi: 10.1016/J.SEMCANCER.2020.11.018
[21] Su J, Liao T, Ren Z, et al. Polydopamine nanoparticles coated with a metal-polyphenol network for enhanced photothermal/chemodynamic cancer combination therapy. Int J Biol Macromol. 2023;238:124088. doi: 10.1016/j.ijbiomac.2023.124088
[22] Ganesh Kumar A, Pugazhenthi E, Sankarganesh P, et al. Microfibrillated cellulose from pine cone: extraction, properties, and characterization. Biomass Convers Biorefin. 2023;13:1–8. doi: 10.1007/s13399-021-01794-2
[23] Chen X, Li Y, Lin Q, et al. Tea polyphenols induced apoptosis of breast cancer cells by suppressing the expression of Survivin. Sci Rep. 2014;4(4). doi: 10.1038/srep04416
[24] Velsankar K, Parvathy G, Sankaranarayanan K, et al. Green synthesis of silver oxide nanoparticles using Panicum miliaceum grains extract for biological applications. Adv Powder Technol. 2022;33:103645. doi: 10.1016/j.apt.2022.103645
[25] Taha KK, Modwi A, Elamin MR, et al. Impact of Hibiscus extract on the structural and activity of sonochemically fabricated ZnO nanoparticles. J Photochem Photobiol A Chem. 2020;390:112263. doi: 10.1016/j.jphotochem.2019.112263
[26] Deshpande SS, Veeragoni D, Rachamalla HK, et al. Anticancer properties of ZnO-Curcumin nanocomposite against melanoma cancer and its genotoxicity profiling. J Drug Deliv Sci Technol. 2022;75:103703. doi: 10.1016/j.jddst.2022.103703
[27] Umavathi S, Subash M, Gopinath K, et al. Facile synthesis and characterization of ZnO nanoparticles using Abutilon indicum leaf extract: An eco-friendly nano-drug on human microbial pathogens. J Drug Deliv Sci Technol. 2021;66:102917. doi: 10.1016/j.jddst.2021.102917
[28] Deivanathan SK, Thomas J, Prakash J, et al. Bio-synthesis of silver nanoparticles using leaf extract of Rhaphidophora pertusa and its characterization, antimicrobial, antioxidant and cytotoxicity activities. Res Chem Intermed. 2023;49(2):423–439. doi: 10.1007/s11164-022-04888-2
[29] Sivakumari G, Rajarajan M, Senthilvelan S. Microwave-assisted synthesis and characterization of activated carbon–zirconium-incorporated CeO2 nanocomposites for photocatalytic and antimicrobial activity. Res Chem Intermed. 2023;49:3539–3561. doi: 10.1007/s11164-023-04968-x
[30] Shehata EMM, Gowayed MA, El-Ganainy SO, et al. Pectin coated nanostructured lipid carriers for targeted piperine delivery to hepatocellular carcinoma. Int J Pharm. 2022;619:121712. doi: 10.1016/j.ijpharm.2022.121712
[31] Shome S, Das Talukdar A, Nath R, et al. Curcumin-ZnO nanocomposite mediated inhibition of Pseudomonas aeruginosa biofilm and its mechanism of action. J Drug Deliv Sci Technol. 2023;81:104301. doi: 10.1016/j.jddst.2023.104301
[32] Greeshma KP, Thamizselvi R. Phytogenic synthesis of ZnO nanoparticles from Catharanthus Roseus and Mori nda Citrifolia leaf extract and its promising multifunctional biological applications. J Drug Deliv Sci Technol. 2023;87:104785. doi: 10.1016/j.jddst.2023.104785
[33] Schröder L, Marahrens P, Koch JG, et al. Effects of green tea, matcha tea and their components epigallocatechin gallate and quercetin on MCF–7 and MDA-MB-231 breast carcinoma cells. Oncol Rep. 2018;41:387–396. doi: 10.3892/or.2018.6789
[34] Devkota HP, Gaire BP, Hori K, et al. The science of matcha: Bioactive compounds, analytical techniques and biological properties. Trends Food Sci Technol. 2021;118:735–743. doi: 10.1016/j.tifs.2021.10.021
[35] Kochman J, Jakubczyk K, Antoniewicz J, et al. Health benefits and chemical composition of matcha green Tea: a review. Molecules. 2021;26(1):85. doi: 10.3390/molecules26010085
[36] Lizoňová D, Hládek F, Chvíla S, et al. Surface stabilization determines macrophage uptake, cytotoxicity, and bioactivity of curcumin nanocrystals. Int J Pharm. 2022;626:122133. doi: 10.1016/j.ijpharm.2022.122133
[37] Sekowski S, Terebka M, Veiko A, et al. Epigallocatechin gallate (EGCG) activity against UV light-induced photo damages in erythrocytes and serum albumin—theore tical and experimental studies. J Photochem Photobiol A Chem. 2018;356:379–388. doi: 10.1016/j.jphotochem.2018.01.018
[38] Keckstein S, Tilgener C, Jeschke U, et al. Effects of matcha tea extract on cell viability and peroxisome proliferator-activated receptor γ expression on T47D breast cancer cells. Arch Gynecol Obstet. 2022;306:451–459. doi: 10.1007/s00404-021-06381-4
[39] Farhan M. Green Tea catechins: nature's Way of preventing and treating cancer. Int J Mol Sci. 2022;23(18):10713. doi: 10.3390/ijms231810713
[40] Zhang W, Cho WC, Bloukh SH, et al. An overview on the exploring the interaction of inorganic nanoparticles with microtubules for the advancement of cancer therapeutics. Int J Biol Macromol. 2022;212:358–369. doi: 10.1016/j.ijbiomac.2022.05.150
[41] Abed NN, Abou El-Enain IMM, El-Husseiny Helal E, et al. Novel biosynthesis of tellurium nanoparticles and investigation of their activity against common pathogenic bacteria. J Taibah Univ Med Sci. 2023;18(2):400–412. doi: 10.1016/J.JTUMED.2022.10.006
[42] Tulbah AS. In vitro bio-characterization of solid lipid nanoparticles of favipiravir in A549 human lung epithelial

cancer cells. J Taibah Univ Med Sci. 2023;18:1076–1086. doi: 10.1016/J.JTUMED.2023.02.014
[43] Shakib P, Mirzaei SZ, Lashgarian HE, et al. Preparation of zinc oxide nanoparticles assisted by okra mucilage and Evaluation of its biological activities. Curr Drug Discov Technol. 2023;20; doi: 10.2174/1570163820666221201090006
[44] Karkhane M, Lashgarian HE, Mirzaei SZ, et al. Antifungal, antioxidant and photocatalytic activities of zinc nanoparticles synthesized by Sargassum vulgare extract. Biocatal Agric Biotechnol. 2020;29:101791. doi: 10.1016/j.bcab.2020.101791
[45] Gilavand F, Saki R, Zahra Mirzaei S, et al. Green synthesis of zinc nanoparticles using aqueous extract of magnoliae officinalis and assessment of its bioactivity potentials. Biointerface Res Appl Chem. 2020;11(1):7765–7774. doi: 10.33263/BRIAC111.77657774
[46] Cheraghipour K, Khalaf AK, Moradpour K, et al. Synthesis, characterization, and antiparasitic effects of zinc oxide nanoparticles-eugenol nanosuspension against Toxoplasma gondii infection. Heliyon. 2023;9(8):e19295. doi: 10.1016/j.heliyon.2023.e19295
[47] Ullah A, Saadullah M, Alvi F, et al. Synergistic effect of silver doped ZnO nanomaterials enhances the anticancer potential against A459 lung cancer cells. J King Saud Univ Sci. 2022;34:101724. doi: 10.1016/j.jksus.2021.101724
[48] Yadav S, Sadique MA, Pal M, et al. Cytotoxicity and DNA fragmentation-mediated apoptosis response of hexagonal ZnO nanorods against human prostate cancer cells. Appl Surf Sci Advan. 2022;9:100237. doi: 10.1016/j.apsadv.2022.100237
[49] Panigrahi G, Medhi H, Wasnik K, et al. Hollow mesoporous SiO2–ZnO nanocapsules and effective in vitro delivery of anticancer drugs against different cancers with low doses of drugs. Mater Chem Phys. 2022;287:126287. doi: 10.1016/j.matchemphys.2022.126287
[50] Hussein BY, Mohammed AM. Green synthesis of ZnO nanoparticles in grape extract: their application as anticancer and anti-bacterial. Mater Today Proc. 2021;42:A18–A26. doi: 10.1016/j.matpr.2021.03.729
[51] AbuMousa RA, Baig U, Gondal MA, et al. Investigation of the survival viability of cervical cancer cells (HeLa) under visible light induced photo-catalysis with facile synthesized WO3/ZnO nanocomposite. Saudi J Biol Sci. 2020;27:1743–1752. doi: 10.1016/j.sjbs.2020.04.038
[52] Murali M, Manjula S, Shilpa N, et al. Facile synthesis of ZnO-NPs from yellow creeping daisy (Sphagneticola trilobata L.) attenuates cell proliferation by inducing cellular level apoptosis against colon cancer. J King Saud Univ Sci. 2022;34:102084. doi:10.1016/j.jksus.2022.102084
[53] Jevapatarakul D, T-Thienprasert J, Payungporn S, et al. Utilization of Cratoxylum formosum crude extract for synthesis of ZnO nanosheets: characterization, biological activities and effects on gene expression of nonmelanoma skin cancer cell. Biomed Pharmacother. 2020;130:110552. doi: 10.1016/j.biopha.2020.110552
[54] Eswari KM, Asaithambi S, Karuppaiah M, et al. Green synthesis of ZnO nanoparticles using Abutilon Indicum and Tectona Grandis leaf extracts for evaluation of anti-diabetic, anti-inflammatory and in-vitro cytotoxicity activities. Ceram Int. 2022;48(22):33624–33634. doi: 10.1016/j.ceramint.2022.07.308
[55] Nava OJ, Luque PA, Gómez-Gutiérrez CM, et al. Influence of Camellia sinensis extract on Zinc Oxide nanoparticle green synthesis. J Mol Struct. 2017;1134:121–125. doi: 10.1016/j.molstruc.2016.12.069
[56] Çolak H. Siyah Çay (camellia sinensis) sulu ekstraktı kullanılarak nanotanecikli ZnO İnce filminin Üretilmesi ve karakterize edilmesi. Iğdır Üniversitesi Fen Bilimleri Enstitüsü Dergisi. 2018;8(4):163–170. doi: 10.21597/JIST.409028
[57] Gonzalez RC, Woods RE, Digital image processing third edition Pearson international edition prepared by Pearson Education. Upper Saddle River, NJ: Prentice Hall; n.d.
[58] Haralick RM, Dinstein I, Shanmugam K. Textural features for image classification. EEE Trans Syst Man Cybern. 1973;SMC-3(6):610–621. doi: 10.1109/TSMC.1973.4309314
[59] Duran H, Alkan FÜ, Ulkay MB, et al. Investigation of the in vitro cytotoxic effects and wound healing activity of ternary composite substance (hollow silica sphere/gum arabic/methylene blue). Int J Biol Macromol. 2019;121:1194–1202. doi: 10.1016/j.ijbiomac.2018.10.098
[60] Alamdari S, Mirzaee O, Nasiri Jahroodi F, et al. Green synthesis of multifunctional ZnO/chitosan nanocomposite film using wild Mentha pulegium extract for packaging applications. Surf Interfaces. 2022;34:102349. doi: 10.1016/j.surfin.2022.102349
[61] Karakuş S, Baytemir G, Özeroğlu CN. An ultra-sensitive smartphone-integrated digital colorimetric and electrochemical Camellia sinensis polyphenols encapsulated CuO nanoparticles-based ammonia biosensor. Inorg Chem Commun. 2022;143:109733. doi: 10.1016/j.inoche.2022.109733
[62] Goudarzi A, Zabihi E, Shahrampour D, et al. Eco-friendly synthesis of large band gap ZnO nanoparticles by trisodium citrate: investigation of annealing effect on structural and optical properties. J Mater Sci Mater Electron. 2022;33:22798–22809. doi: 10.1007/s10854-022-09047-2
[63] Aga KW, Efa T, Beyene TT. Effects of sulfur doping and temperature on the energy Bandgap of ZnO Nanoparticles and Their Antibacterial Activities. ACS Omega. 2022;7:10796–10803. doi: 10.1021/acsomega.2c00647
[64] Xiao J, Zou C, Liu M, et al. Mixing in a soft-elastic reactor (SER) characterized using an RGB based image analysis method. Chem Eng Sci. 2018;181:272–285. doi: 10.1016/j.ces.2018.02.019
[65] Guo G, Zheng Q, Li T, et al. 3D printed self-calibrating on-site sensing platform based on bimodal excitation carbon dots for visual 4-nitrophenol detection by means of the localization of inner filter effect and pH regulation. Chem Eng Sci. 2023;281:119201. doi: 10.1016/j.ces.2023.119201
[66] Panckow RP, Bliatsiou C, Nolte L, et al. Characterisation of particle stress in turbulent impeller flows utilising photo-optical measurements of a flocculation system – PART 1. Chem Eng Sci. 2023;267:118333. doi: 10.1016/j.ces.2022.118333
[67] Thomas S, Gunasangkaran G, Arumugam VA. Synthesis and characterization of zinc oxide nanoparticles of solanum nigrum and its anticancer activity via the induction of apoptosis in cervical cancer. Biol Trace Elem Res. 2022;200(6):2684–2697. doi: 10.1007/s12011-021-02898-6
[68] Naiel B, Fawzy M, Halmy MWA, et al. Green synthesis of zinc oxide nanoparticles using Sea Lavender (Limonium pruinosum L. Chaz.) extract: characterization, evaluation of anti-skin cancer, antimicrobial and antioxidant potentials. Sci Rep. 2022;12(1):1–12. doi: 10.1038/s41598-022-24805-2

[69] Ilangovan A, Venkatramanan A, Thangarajan P, et al. Green synthesis of zinc oxide nanoparticles (ZnO NPs) using aqueous extract of tagetes erecta flower and evaluation of its antioxidant, antimicrobial, and cytotoxic activities on HeLa cell line. Curr Biotechnol. 2021;10:61–76. doi: 10.2174/2211550109999201202123939

[70] El-Waseif AA, El-Ghwas DE. Anti-breast cancer and cytotoxicity of nano materials formed bacterial cellulose-ZnO-Ag composite. Mater Today Proc. 2022;60:1651–1655. doi: 10.1016/j.matpr.2021.12.193

[71] Anitha J, Selvakumar R, Hema S, et al. Facile green synthesis of nano-sized ZnO using leaf extract of Morinda tinctoria: MCF-7 cell cycle arrest, antiproliferation, and apoptosis studies. J Ind Eng Chem. 2022;105:520–529. doi: 10.1016/j.jiec.2021.10.008

[72] Shahriary S, Tafvizi F, Khodarahmi P, et al. Phyto-mediated synthesis of CuO nanoparticles using aqueous leaf extract of Artemisia deserti and their anticancer effects on A2780-CP cisplatin-resistant ovarian cancer cells. Biomass Convers Biorefin. 2022;1:1–17. doi: 10.1007/S13399-022-02436-X/FIGURES/11

[73] Resmi R, Yoonus J, Beena B. A novel greener synthesis of ZnO nanoparticles from Nilgiriantusciliantus leaf extract and evaluation of its biomedical applications. Mater Today Proc. 2021;46:3062–3068. doi: 10.1016/j.matpr.2021.02.498

[74] Barreira S, Moutinho C, Silva AMN, et al. Phytochemical characterization and biological activities of green tea (Camellia sinensis) produced in the Azores, Portugal. Portugal, Phytomedicine Plus. 2021;1:100001. doi: 10.1016/j.phyplu.2020.100001

[75] Fan D-M, Fan K, Yu C-P, et al. Tea polyphenols dominate the short-term tea (Camellia sinensis) leaf litter decomposition. J Zhejiang Univ Sci B. 2017;18(2):99–108. doi: 10.1631/jzus.B1600044

[76] Ravindranath MH, Saravanan TS, Monteclaro CC, et al. Epicatechins purified from green Tea (camellia sinensis) differentially suppress growth of gender-dependent human cancer cell lines. eCAM. 2006;3:237–247. doi: 10.1093/ecam/nel003

[77] Xiang L-P, Wang A, Ye J-H, et al. Suppressive effects of Tea catechins on breast cancer. Nutrients. 2016;8(8):458. doi: 10.3390/nu8080458

[78] Wang Y, Jin HY, Fang MZ, et al. Epigallocatechin gallate inhibits dimethylhydrazine-induced colorectal cancer in rats. World J Gastroenterol. 2020;26:2064–2081. doi: 10.3748/wjg.v26.i17.2064

[79] Hayakawa S, Ohishi T, Miyoshi N, et al. Anti-Cancer effects of green Tea epigallocatchin-3-gallate and coffee chlorogenic acid. Molecules. 2020;25(19):4553. doi: 10.3390/molecules25194553

[80] Shirakami Y, Shimizu M. Possible mechanisms of green Tea and Its constituents against cancer. Molecules. 2018;23(9):2284. doi: 10.3390/molecules23092284

[81] Sharifi-Rad M, Pezzani R, Redaelli M, et al. Preclinical activities of epigallocatechin gallate in signaling pathways in cancer. Molecules. 2020;25(3):467), doi: 10.3390/molecules25030467

[82] Bisht G, Rayamajhi S. Zno nanoparticles: A promising anticancer agent. Nanobiomedicine (Rij). 2016;3. doi: 10.5772/63437/ASSET/IMAGES/LARGE/10.5772_63437-FIG3.JPEG

[83] Tabrez S, Khan AU, Hoque M, et al. Biosynthesis of ZnO NPs from pumpkin seeds' extract and elucidation of its anticancer potential against breast cancer. Nanotechnol Rev. 2022;11:2714–2725. doi: 10.1515/ntrev-2022-0154

[84] Al-Ghamdi SA, Alkathiri TA, Alfarraj AE. Green synthesis and characterization of zinc oxide nanoparticles using Camellia sinensis tea leaf extract and their antioxidant, anti-bactericidal and anticancer efficacy. Res Chem Intermed. 2022;48(11):4769–4783. doi: 10.1007/s11164-022-04845-z

[85] Saeed F, Younas M, Fazal H. Green and chemically synthesized zinc oxide nanoparticles: effects on in-vitro seedlings and callus cultures of*Silybum marianum*and evaluation of their antimicrobial and anticancer potential. Artif Cells Nanomed Biotechnol. 2021;49:450–460. doi: 10.1080/21691401.2021.1926274

[86] Pavithra M, Jessie Raj MB. Synthesis of ultrasonic assisted co-precipitated Ag/ZnO nanorods and their profound anti-liver cancer and antibacterial properties. Mater Sci Eng B. 2022;278:115653. doi: 10.1016/j.mseb.2022.115653

[87] Truong Hoang Q, Ravichandran V, Nguyen Cao TG, et al. Piezoelectric Au-decorated ZnO nanorods: Ultrasound-triggered generation of ROS for piezocatalytic cancer therapy. Chem Eng J. 2022;435:135039. doi: 10.1016/j.cej.2022.135039

[88] Ali S, Govindaraj Sudha K, Karunakaran G, et al. Anticancer and photocatalytic activities of zinc oxide nano rods synthesized from Manilkara littoralis leaf extract. Mater Chem Phys. 2022;277:125541. doi: 10.1016/j.matchemphys.2021.125541

[89] Wahab R, Khan F, Kaushik N, et al. L-cysteine embedded core-shell ZnO microspheres composed of nanoclusters enhances anticancer activity against liver and breast cancer cells. Toxicol in Vitro. 2022;85:105460. doi: 10.1016/j.tiv.2022.105460